Structural basis for the recognition of nectin-like protein-5 by the human-activating immune receptor, DNAM-1

Received for publication, May 9, 2019, and in revised form, June 27, 2019 Published, Papers in Press, June 28, 2019, DOI 10.1074/jbc.RA119.009261

Felix A. Deuss[‡], Gabrielle M. Watson[‡§], Katharine J. Goodall[¶], Isobel Leece[¶], Sayantani Chatterjee[‖], Zhihui Fu[‡], Morten Thaysen-Andersen[‖], Daniel M. Andrews[¶], Jamie Rossjohn[‡§1], and Richard Berry[‡§2]**

*From the [‡]Infection and Immunity Program and Department of Biochemistry and Molecular Biology, Biomedicine Discovery Institute, Monash University, Clayton, Victoria 3800, Australia, the [§]Australian Research Council Centre of Excellence in Advanced Molecular Imaging, Monash University, Clayton, Victoria 3800, Australia, the [¶]Department of Immunology and Pathology, Central Clinical School, Monash University, Melbourne, Victoria 3800, Australia, the [‖]Department of Molecular Sciences, Faculty of Science and Engineering, Macquarie University New South Wales 2109, Australia, and the **Institute of Infection and Immunity, Cardiff University School of Medicine, Heath Park, Cardiff CF14 4XN, United Kingdom*

Edited by Peter Cresswell

Nectin and nectin-like (Necl) adhesion molecules are broadly overexpressed in a wide range of cancers. By binding to these adhesion molecules, the immunoreceptors DNAX accessory molecule-1 (DNAM-1), CD96 molecule (CD96), and T-cell immunoreceptor with Ig and ITIM domains (TIGIT) play a crucial role in regulating the anticancer activities of immune effector cells. However, within this axis, it remains unclear how DNAM-1 recognizes its cognate ligands. Here, we determined the structure of human DNAM-1 in complex with nectin-like protein-5 (Necl-5) at 2.8 Å resolution. Unexpectedly, we found that the two extracellular domains (D1–D2) of DNAM-1 adopt an unconventional "collapsed" arrangement that is markedly distinct from those in other immunoglobulin-based immunoreceptors. The DNAM-1/Necl-5 interaction was underpinned by conserved lock–and– key motifs located within their respective D1 domains, but also included a distinct interface derived from DNAM-1 D2. Mutation of the signature DNAM-1 "key" motif within the D1 domain attenuated Necl-5 binding and natural killer cell–mediated cytotoxicity. Altogether, our results have implications for understanding the binding mode of an immune receptor family that is emerging as a viable candidate for cancer immunotherapy.

The activity of immune effector cells is tightly regulated to enable the identification and elimination of infected, transformed, or stressed cells while preventing autoimmunity toward the surrounding healthy tissue. This specificity is achieved by the coordinated activity of a variety of cell surface–bound receptors that either stimulate or dampen immune cell activation. For example, natural killer (NK)[3] cell function is regulated by the integration of signals derived from a variety of paired receptor families that include the Ly49 receptors in rodents (1), the killer cell and leukocyte immunoglobulin receptors (KIRs and LIRs, respectively) in humans (2, 3), and the CD94-NKG2 (4) and NKR-P1 (5) families in both species. Within these systems, the inhibitory receptors typically recognize "self"-molecules that are broadly expressed on the surface of healthy cells (6–10), while their stimulatory counterparts predominantly bind to nonself or stress-induced ligands (11–13).

Alternatively, some paired receptor families comprise members that exhibit overlapping ligand specificities, and as such they compete with each other to fine-tune the immune response. For example, the nectin receptors DNAM-1 (CD226), CD96 (TACTILE), and T-cell immunoglobulin and immunoreceptor tyrosine-based inhibitory motif (TIGIT) are expressed on T and NK cells, where they mediate effector/target cell adhesion and immune synapse formation and regulate effector function (14). Within this context, DNAM-1 is a stimulatory receptor that was first identified by its ability to activate T cells independently of T-cell receptor engagement (15–19). DNAM-1 has since been shown to be critical for tumor immunosurveillance, as demonstrated in mouse models of chemically-induced tumors, and by DNAM-1$^{-/-}$ mice, which exhibit accelerated tumor growth (17). In contrast, TIGIT is an inhibitory receptor (20–22), and CD96 is able to counter-balance DNAM-1 function in mice (16), although human CD96 has been reported to stimulate NK cell cytotoxicity (23).

This work was supported by a Macquarie University Research Seeding grant (to M. T.-A.), International Macquarie University Research Excellence Scholarship iMQRES 2017152 (to S. C.), Australian Research Council Laureate Fellowship FL160100049 (to J. R.), and by Career Development Fellowship APP1109901 from the National Health and Medical Research Council of Australia (to R. B.). The authors declare that they have no conflicts of interest with the contents of this article.

This article contains Figs. S1–S7 and Tables S1–S3.

The atomic coordinates and structure factors (code 6O3O) have been deposited in the Protein Data Bank (http://wwpdb.org/).

[1] Joint senior author. To whom correspondence may be addressed. Tel.: 61-3-9902-9236; Fax: 99054699; E-mail: jamie.rossjohn@monash.edu.

[2] Joint senior author. To whom correspondence may be addressed. Tel.: 61-3-9902-9239; E-mail: richard.berry@monash.edu.

[3] The abbreviations used are: NK, natural killer; DNAM-1, DNAX accessory molecule-1; Necl, nectin and nectin-like; TIGIT, T-cell immunoreceptor with Ig and ITIM domain; KIR, killer cell immunoglobulin receptor; LIR, leukocyte immunoglobulin receptor; DMEM, Dulbecco's modified Eagle's medium; FCS, fetal calf serum; PVDF, polyvinylidene difluoride; PGC, porous graphitized carbon; ACN, acetonitrile; FA, formic acid; AUC, area-under-the-curve; EIC, extracted ion chromatogram; HILIC-SPE, hydrophilic interaction LC–solid-phase extraction; NCE, normalized collision energy; endo H, endoglycosidase H; SPR, surface plasmon resonance; HCD, higher-energy C-trap dissociation; FWHM, full width at half-maximum; PDB, Protein Data Bank; r.m.s.d., root mean square deviation; AGC, automatic gain control; HCD, higher-energy C-trap dissociation.

Nectin receptor function depends on their capacity to recognize certain nectin and nectin-like (Necl) adhesion molecules, namely nectin-2 (CD112) and Necl-5 (CD155), which are broadly overexpressed in a wide range of cancers (24–27). During homeostasis, nectin (like) proteins tether adjacent cells together via the formation of homo- and heterodimers. These interactions rely on signature "lock" (AX_6G) and "key" (T(F/Y)P) motifs located within their most membrane distal (D1) domains (28). The nectin receptors also contain similar lock and key motifs within their D1 domains, although they differ in the complexity of their ectodomains. For example, TIGIT, DNAM-1, and CD96 possess one, two, and three extracellular Ig domains, respectively. Structural studies of TIGIT and CD96 have indicated that their D1 domains, which are sufficient for ligand binding, engage their cognate ligands by a docking mode that mimics nectin homo/heterodimerization (29–31). A recent structure of mouse DNAM-1 bound to human Necl-5 supports this proposition, but it also indicated that the second DNAM-1 domain (D2) can modulate the interaction (32). However, the molecular basis underpinning recognition of Necl-5 by human DNAM-1 remains unclear.

Here, we determined the structure of human DNAM-1 in complex with one of its cognate ligands, Necl-5. DNAM-1 bound Necl-5 in a 1:1 stoichiometry via a docking mode that enabled the interaction between lock and key motifs within their respective D1 domains. The unconventional "collapsed" architecture of the two extracellular domains of DNAM-1 positioned the D2 domain such that it made direct contacts with Necl-5. Binding and functional studies indicated that residues within DNAM-1 D2 did not modulate the interaction with ligands or functional response of DNAM-1 to Necl-5/nectin-2–expressing target cells. In contrast, the D1-localized key residue was critical for DNAM-1–dependent ligand binding and NK cell cytotoxicity. Altogether, these data expand our understanding of the molecular features that govern nectin receptor–ligand interactions.

Results

Structural determination of the DNAM-1/Necl-5 complex

Although the mode of interaction of TIGIT and CD96 with their cognate ligands has been established (29–31), the structural basis for human DNAM-1 ligand recognition is unknown. To address this gap in our knowledge, we expressed the extracellular Ig domains of human DNAM-1 (D1–D2) and Necl-5 (D1–D3) in human embryonic kidney (HEK)-293S and Hi5 insect cells, respectively. DNAM-1 behaved as a heavily glycosylated monomeric species, as judged by its apparent migration during SDS-PAGE analysis and size-exclusion chromatography (Fig. S1). Necl-5 also appeared to be a glycosylated monomer, consistent with previous studies (30). To aid in crystallization, we treated DNAM-1 with endoglycosidase H (endo H), which trims high-mannose *N*-glycans that are the only glycoforms produced by HEK-293S cells to a single *N*-acetylglucosamine (GlcNAc) residue, prior to mixing with a 1:1 molar ratio of Necl-5. Using this approach, we generated crystals of the DNAM-1/Necl-5 co-complex and determined the structure to 2.8 Å resolution (Table S1). The crystallographic asymmetric unit comprised two molecules of DNAM-1 and two molecules of Necl-5 that formed two similar DNAM-1/Necl-5 heterodimeric complexes (root mean square deviation (r.m.s.d.) of 1.78 over 430 Cα atoms). Although one of the DNAM-1/Necl-5 complexes (chains B and D) was relatively poorly resolved, the electron density for the other heterodimer (chains A and C) was clear, allowing the building of the entire polypeptide chains encompassing the D1 and D2 domains of DNAM-1 (Glu-19–Ala-241) and the D1–D3 domains of Necl-5 (Glu-27–Val-327), with the exception of a single loop in DNAM-1 D1 (Ser-84–Ser-89) and two loops within Necl-5 D3 (Asp-252–Gln-259 and Val-302–Thr-308), none of which were located at the DNAM-1/Necl-5 interface. Indeed, the structure refined well (Fig. S2) to an R_{factor} and R_{free} of 20.8 and 23.0%, respectively, thereby permitting a detailed understanding of the interactions that governed DNAM-1/Necl-5 recognition.

DNAM-1 comprises an atypical configuration of two tandem Ig domains

DNAM-1 was composed of two Ig-variable domains that were tethered together by a relatively long 12-amino acid linker region (Gln-126–Asn-137) (Fig. 1*A*). Six individual GlcNAc residues were visible attached to Asn residues 32, 83, 90, and 97 within D1 and Asn-147 and -186 within D2. The DNAM-1 D1 domain was composed of one small (sheet I: BED) and one large (sheet II: AGFCC′C″) β-sheet that were bridged by a single disulfide bond located between the B- and F-strands (Cys-37–Cys-108) (Fig. 1*B*). DNAM-1 D2 was organized similarly to the D1 domain (r.m.s.d. 2.6 Å over 63 Cα atoms), whereby it possessed a canonical disulfide bond, linking the B- and F-strands (Cys-152–Cys-222). However, within the D2 domain, the regions equivalent to the C″- and D-strand were no longer H-bonded to sheets I and II, respectively, due in part to an additional disulfide bond that attached the C′-strand to the C′–D linker (Cys-179–Cys-199).

Within the DNAM-1 structure, the D1 and D2 domains were collapsed on each other in an unusual side–by–side arrangement, such that the β-strands of D1 and D2 formed a single extended β-sheet (Fig. 1, *A* and *B*). This unexpected architecture, where D2 was rotated relative to D1 by ~100°, was facilitated by the extended nature of the inter-domain linker that connected the G-strand of D1 to the A-strand of D2. The DNAM-1 D1/D2 interface occupied a moderate solvent-inaccessible surface area (≈900 Å^2) and was primarily hydrophobic in nature (Fig. 1*C*). The core of the interaction zone was derived from the A-strand of D1 and the C′-strand of D2, where four contiguous H-bonds between the main chain atoms of Trp-23–Val-27 (D1) and Ile-173–Leu-175 (D2) formed an anti-parallel β-sheet that stitched the D1 and D2 domains together (Fig. 1*D* and Table S2). The interface was further supported by the DNAM-1 N terminus, where Leu-22–His-24 interacted with several residues that spanned the length of the C and C′ strands of D2 (Fig. 1*E*).

Notably, the relative juxtapositioning of DNAM-1 domains is completely distinct to the "beads-on-a-string" arrangement evident within the nectin (-like) ligands (Fig. 2), to which the nectin receptors were previously considered to be closely structurally related. Indeed, although many immune receptors are

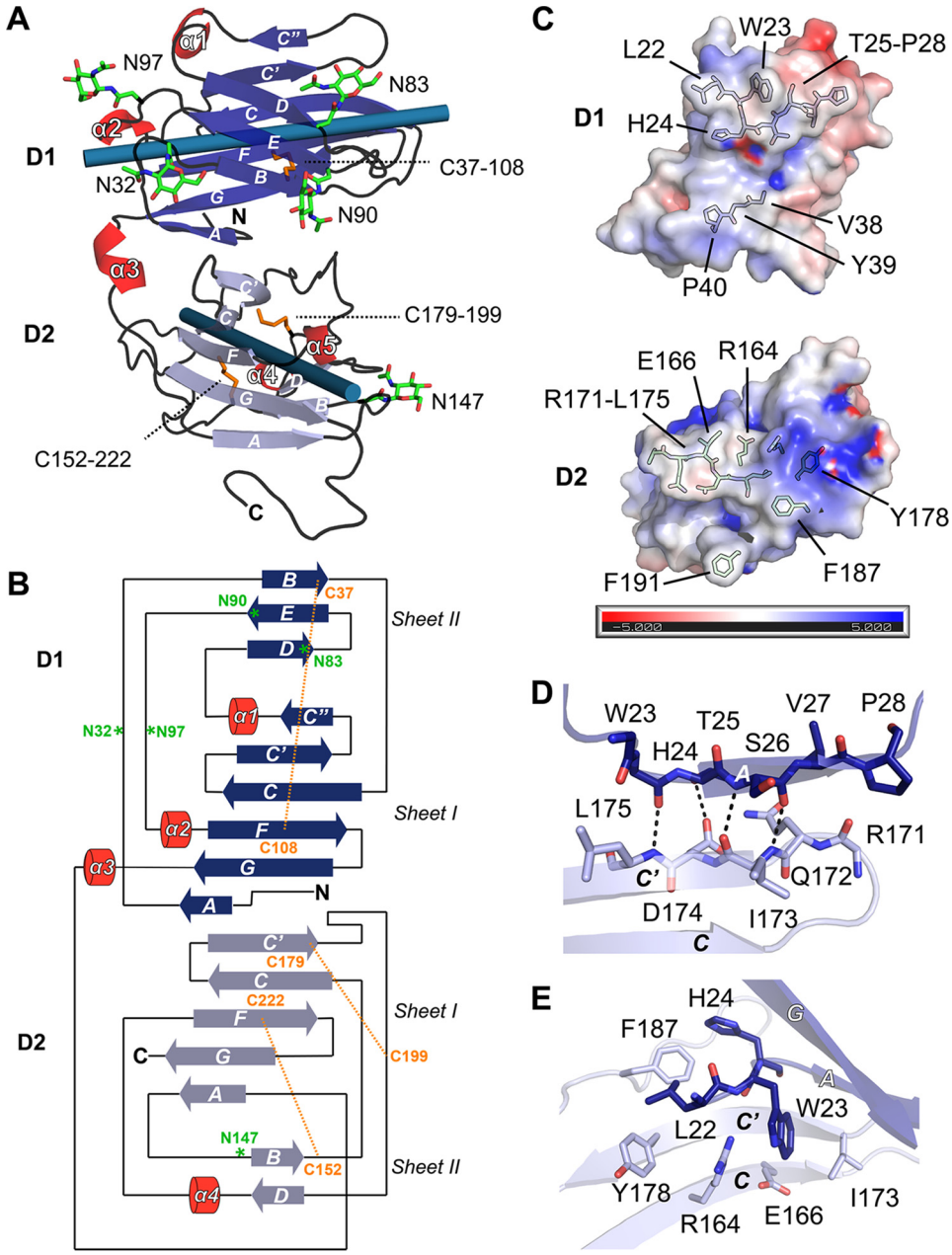

Figure 1. Atypical stacked architecture of DNAM-1. *A,* overview of the structure of human DNAM-1. The β-strands of D1 and D2 are colored in *dark* and *light blue,* respectively, helices are colored *red*; disulfide bonds are shown as *orange sticks*, and *N*-linked glycans are represented by *green sticks*. *Cylinders* represent the axis of inertia of each domain. *B,* topology diagram of DNAM-1 colored as in *A*. *C,* electrostatic surface potential of DNAM-1 D1 and D2 domains (*blue,* electropositive; *red,* electronegative). Residues that are involved in the D1/D2 interface are shown as *sticks*. *D* and *E,* close-up views of the DNAM-1 D1/D2 interface. *Dashed lines* represent H-bonds.

composed of multiple tandem Ig domains, the inter-domain angles are typically large (>75°), resulting in either linear (PD1-L2) (33), perpendicular (LIR-B1) (34), or open V-shaped (NKp46 and KIR3DL1) (9, 35) configurations (Fig. 2). Among the immune receptors, the DNAM-1 architecture is most similar to that found in FcγRIIA (36), although the rotational angle between D1 and D2 domains within these two receptors is quite distinct. Notably, the overall architecture of DNAM-1 reported here is similar to that of (unliganded) human and mouse DNAM-1 recently reported by Wang *et al.* (32) (r.m.s.d. 0.79 and 1.37 Å over 170 and 185 aligned Cα atoms, respectively), indicating that this unusual domain configuration represents the *bona fide* native state of DNAM-1. Accordingly, DNAM-1 possessed a collapsed side–by–side architecture that is atypical among immune receptors whose structures have been solved to date.

Overview of the DNAM-1/Necl-5 heterodimer

DNAM-1 bound exclusively to the D1 domain of Necl-5 via an extensive interface that buried a total solvent-inaccessible surface area of ~1880 Å^2 and was characterized by high shape complementarity (Sc = 0.79). Within the complex, Necl-5 adopted a linear configuration of its three Ig domains, such that the D2 and D3 domains projected away from DNAM-1 and did

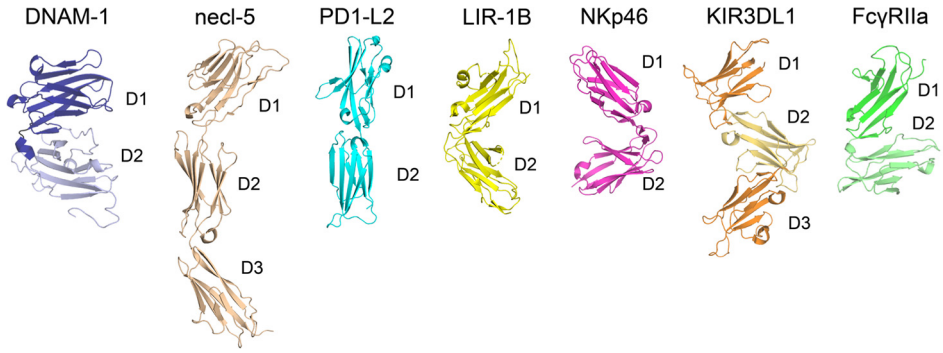

Figure 2. Structural comparison of immune receptors that comprise multiple tandem Ig domains. From *left to right*, PDB codes: 6O3O (DNAM-1); necl-5 (withdrawn); 3BP5 (PD1-L2); 4NO0 (LIR-B1); 1P6F (NKp46); 3VH8 (KIR3DL1); and 1FCG (FcγRIIa).

not participate in the interaction (Fig. 3*A*). Although some subtle differences in the inter-domain angle were evident, the overall architecture of Necl-5 was similar to that previously described for the unbound and CD96-bound forms (Fig. S3) (28, 30). In this arrangement, the C termini of both receptor and ligand are positioned at opposing ends of the complex (Fig. 3*A*). Accordingly, the DNAM-1/Necl-5 interaction could conceivably occur either in *cis* or in *trans*, *i.e.* between molecules located on single or adjacent cellular membranes, respectively (Fig. 3*B*). Although a higher-order heterotetrameric arrangement was visible within the crystal lattice (Fig. S4), we do not consider this to be a physiologically relevant assembly because the interface was mediated solely by interactions between two DNAM-1 monomers, and DNAM-1 was judged to be monomeric in solution (Fig. S1*A*).

DNAM-1 D1 binds to Necl-5 via a conserved docking mode

The DNAM-1/Necl-5 interface was primarily centered around DNAM-1 D1, which engaged Necl-5 via a head–to–head docking mode reminiscent of that utilized by TIGIT and CD96 (Fig. S5) (29, 31). Here, DNAM-1 D1 interacted with necl-5 in an orthogonal orientation across the breadth of their respective AGFCC′C″ sheets, giving this region of the interface a pseudo 2-fold symmetrical appearance (Fig. 3*A*). The defining feature of this region of the interface was derived from the lock and key motifs, whereby aromatic key residues within the F-G loop of both DNAM-1 (Tyr-113) and Necl-5 (Phe-128) were inserted into hydrophobic pockets formed by the C′–C″ loops of their respective binding partner (Fig. 3, *C* and *D*, and Table S3). These interactions were further stabilized by the C–C′ loop of each molecule, which flexed inward to enable a single residue (Gln-57 in DNAM-1 and Ser-74 in Necl-5) to make interactions with the G-strand of the binding partner (Fig. 3*E*). Together, these two major points of contact served to latch the molecules together at the periphery of the interface. However, residues located within the central region of this interface also played a prominent role and accounted for 8 of the 11 total H-bonds (Fig. 3*F*). Here, several residues within the central C-, F-, and G-strands of DNAM-1 and Necl-5 projected directly toward the opposing sheet where they primarily made H-bond interactions with main-chain atoms of their binding partner. Thus, the D1 domain of DNAM-1 binds to Necl-5 via a conserved docking topology that is characteristic of the nectin receptor family.

DNAM-1 D2 makes direct interactions with Necl-5

In addition to the conventional interface derived from their respective D1 domains, we observed an interaction site located between DNAM-1 D2 and Necl-5 D1. This interface contributed a relatively small fraction (13%) of the total buried surface area (Fig. 3*G*) but involved a cluster of direct contacts centered on Asn-186 of DNAM-1 (Fig. 3*H*). Here, Asn-186 lie against the C–C′ loop of Necl-5, where it was involved in multiple interactions with the backbone of Gly-70, Glu-71, and Ser-72. Surprisingly, the GlcNAc remnant of the elongated *N*-linked glycan of Asn-186 also made direct interactions with Necl-5, including an H-bond with Ser-72. The presence of a glycan attached to Asn-186 was clearly supported by the unbiased electron density (Fig. S6*A*) and glycopeptide and glycan analyses of recombinantly produced DNAM-1 without prior endo H treatment (Fig. S6*B*).

Comparison with the mouse DNAM-1/Necl-5 structure

Overall, the docking mode of DNAM-1 onto Necl-5 is conserved between human and mouse DNAM-1 (r.m.s.d. 1.44 Å over 216 aligned Cα atoms) (Fig. S7*A*). However, closer inspection of the interface reveals several subtle differences. In particular, of the 22 human DNAM-1 residues that formed interactions with Necl-5, only seven are conserved in mouse DNAM-1 (Fig. S7*B*). This includes the signature aromatic key (Tyr-113), which is a phenylalanine in mouse DNAM-1. Within the interface, the differences between mouse and human DNAM-1 are most obvious in the D2 domain, where the C′–D loop, which lacks a glycan consensus motif in mouse DNAM-1, adopts distinct conformations within the two structures resulting in altered interactions with the C–C′ loop of Necl-5 (Fig. S7*A*).

Mutations within DNAM-1 D1 but not D2 impact binding to nectin-2 and Necl-5

Next, to investigate the energetic contribution of DNAM-1 D2 to ligand binding, we first attempted to express the DNAM-1 D1 domain in isolation. However, we were unable to produce this truncated protein using mammalian cells, most probably due to instability associated with the exposure of a hydrophobic surface that would normally reside at the D1/D2 interface (Fig. 1*C*). Instead, we generated a panel of DNAM-1 point mutants and assessed their interaction with nectin-2 and Necl-5 using surface plasmon resonance (SPR). Here, both

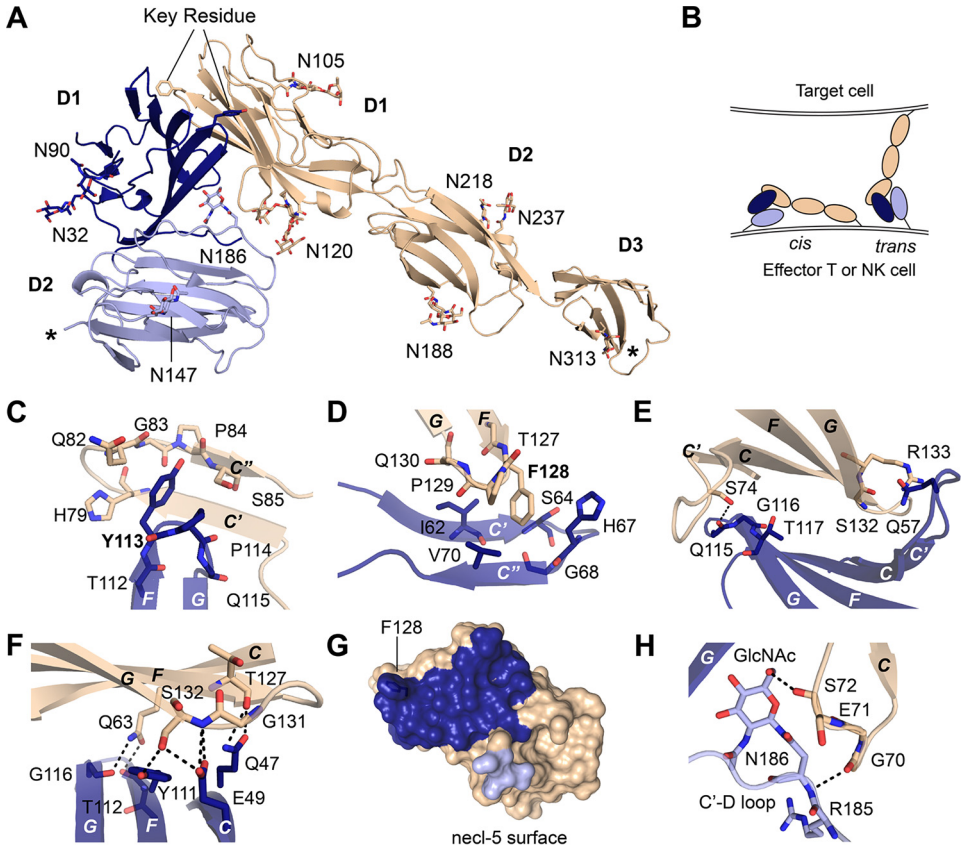

Figure 3. DNAM-1–necl-5 complex. *A,* overview of the structure of DNAM-1 (D1 and D2 colored *dark* and *light blue*, respectively) bound to necl-5 (*tan*). The aromatic key residues (Tyr-113 in DNAM-1; Phe-128 in necl-5) and *N*-glycans are labeled and shown as *sticks*. *Asterisks* denote the C termini. *B,* schematic showing how the DNAM-1/necl-5 complex could exist on the cell surface. *C–F,* close-up views of the DNAM-1 D1–necl-5 interactions focused on the DNAM-1 key (*C*), the necl-5 key (*D*), the C–C′ loops (*E*), and the centrally-located residues (*F*). *G,* binding footprint of DNAM-1 D1 (*dark blue*) and D2 (*light blue*) on necl-5 D1 (*tan*). *H,* view of the DNAM-1 D2/necl-5 interface focused on Asn-186. H-bonds are represented by *dashed lines*.

Necl-5 and nectin-2 bound to WT HEK-293S produced DNAM-1 with comparable affinity (K_D = 1.8 ± 0.6 and 2.9 ± 0.8 μM, respectively) (Fig. 4*A*). Although we were only able to couple lower amounts on to the SPR chip, mutation of the DNAM-1 key residue (Y113A) within the D1 domain drastically reduced nectin-2 and Necl-5 binding when compared with a control mutation (R96A) in a surface-exposed DNAM-1 residue that was distal to the Necl-5– binding site (Fig. 4*A*). However, mutations within DNAM-1 D2 that disrupted Asn-186 and its associated *N*-glycan (N186A) or the glycosylation consensus motif, defined as N*X*(S/T), where $X \neq$ P (T188A), did not markedly impact the binding affinity of DNAM-1 for either nectin-2 or Necl-5 (K_D = 2.0–2.5 μM) (Fig. 4*A*). To further confirm that the nature of the glycan chain attached to Asn-186 did not impact the interaction with Necl-5/nectin-2, we also tested the binding of recombinant DNAM-1 produced in HEK-293T cells, which was decorated with a variety of complex *N*-glycans similar to those that would be expected to occur *in vivo*, as opposed to the more homogeneous high-mannose *N*-glycans of HEK-293S–produced DNAM-1 (Fig. S6*B*). However, the binding of HEK-293T–produced DNAM-1 to Necl-5 and nectin-2 was of similar affinity to DNAM-1 produced in HEK-293S cells (Fig. 4*A*).

To further probe the impact of DNAM-1 mutants in a cellular system, we also tetramerized the biotinylated DNAM-1 mutants and assessed their ability to bind human myelogenous leukemia (K562) cells, which express Necl-5 and nectin-2 (Fig. 4*B*) by flow cytometry. Although no binding was observed using a control murine cell line lacking human DNAM-1 ligands, WT DNAM-1 bound well to the K562 cells (Fig. 4, *C* and *D*). With the exception of the T188A mutant, which exhibited a 68% increase in binding, the overall pattern of binding of the mutant or variant forms of DNAM-1 closely matched that obtained by SPR. The R96A and N186A mutations as well as HEK-293T–produced DNAM-1 bound equivalently to HEK-293S DNAM-1, whereas the Y113A mutation reduced binding to the K562 cells. Thus, the aromatic key residue of DNAM-1 is critical for the interaction with Necl-5 and nectin-2, whereas Asn-186 and its associated *N*-glycan appear to be dispensable for ligand binding under these experimental conditions.

Mutations within DNAM-1 D1, but not D2, impact NK cell killing

Finally, to investigate the functional relevance of DNAM-1/Necl-5 interactions, we transfected WT DNAM-1 (and mutants thereof) into an NK cell line (NK92) that lacked endogenous DNAM-1 expression (Fig. 5*A*) and co-incubated these cells with K562 cells at a range of NK/target cell ratios (Fig. 5*B*). Analysis of the expression of DNAM-1 in these cell lines demonstrated that DNAM-1^{N186A} could not be detected using the anti-DNAM-1 antibody 11A8. Thus, we confirmed the expression of DNAM-1^{N186A} in these cells using nectin-2 tetramers.

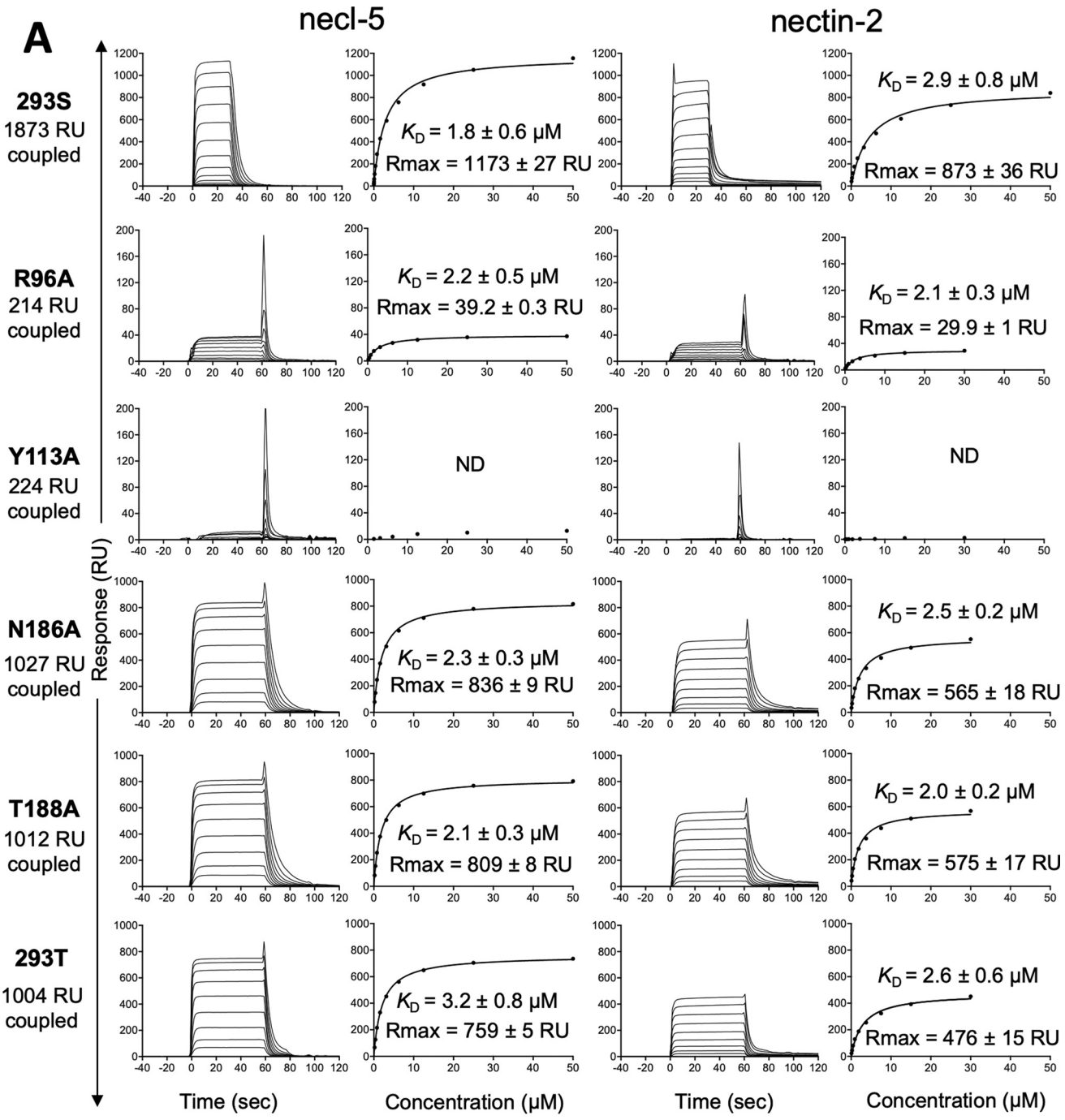
A
necl-5
nectin-2
293S
1873 RU
coupled
K_D = 1.8 ± 0.6 μM
Rmax = 1173 ± 27 RU
K_D = 2.9 ± 0.8 μM
Rmax = 873 ± 36 RU
R96A
214 RU
coupled
K_D = 2.2 ± 0.5 μM
Rmax = 39.2 ± 0.3 RU
K_D = 2.1 ± 0.3 μM
Rmax = 29.9 ± 1 RU
Y113A
224 RU
coupled
ND
ND
N186A
1027 RU
coupled
K_D = 2.3 ± 0.3 μM
Rmax = 836 ± 9 RU
K_D = 2.5 ± 0.2 μM
Rmax = 565 ± 18 RU
T188A
1012 RU
coupled
K_D = 2.1 ± 0.3 μM
Rmax = 809 ± 8 RU
K_D = 2.0 ± 0.2 μM
Rmax = 575 ± 17 RU
293T
1004 RU
coupled
K_D = 3.2 ± 0.8 μM
Rmax = 759 ± 5 RU
K_D = 2.6 ± 0.6 μM
Rmax = 476 ± 15 RU
Response (RU)
Time (sec)
Concentration (μM)
Time (sec)
Concentration (μM)
B
Fluorescent Intensity (arbitrary units)
nectin-2
necl-5
C
Fluorescent Intensity (arbitrary units)
DNAM-1N186A
DNAM-1T188A
DNAM-1Y113A
DNAM-1R96A
DNAM-1293S
DNAM-1293T
Control
Tetramer
D
Median Fluorescent Intensity (arbitrary units)
****
****
Control
DNAM-1293T
DNAM-1293S
DNAM-1R96A
DNAM-1Y113A
DNAM-1T188A
DNAM-1N186A

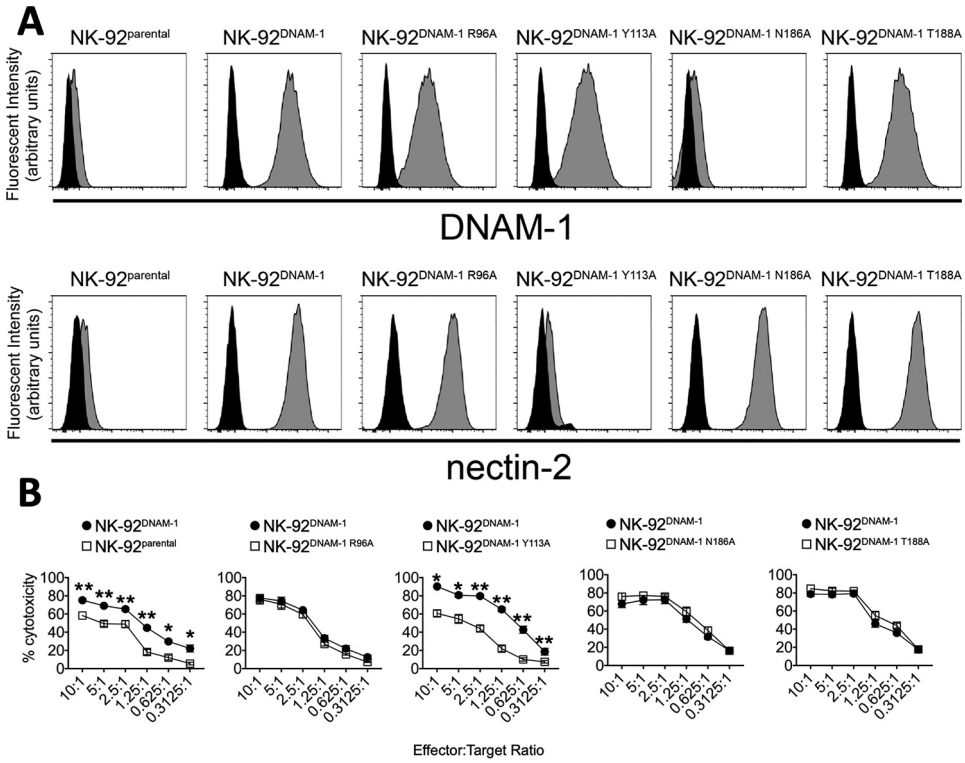

Figure 5. Cytotoxic activity of NK92 cells transduced with DNAM-1 mutants. *A,* NK92 cells expressing WT and mutant DNAM-1 were generated, and the expression of DNAM-1 was assessed by flow cytometry using an anti-DNAM-1 antibody (*top*) or nectin-2 tetramer (*bottom*). For each panel, the *filled black histogram* is either isotype control (*top*) or streptavidin-PE (*bottom*), and the *filled gray histogram* is the specific reagent. The histograms are overlaid and are modal between samples. *B,* parental NK92 cells as well as transfected cells expressing full-length DNAM-1 and the mutant forms were used in cytotoxicity assays. All experiments were performed in the presence of saturating amounts of anti-NKG2D. NK92 cells expressing DNAM-1 demonstrate increased killing of K562 cells relative to parental NK92 cells (*left panel*). Killing of all DNAM-1 mutants are shown relative to WT DNAM-1. Significant differences (determined by the Mann-Whitney test) at each effector/target ratio are indicated by *asterisks* (*, $p < 0.05$; **, $p < 0.005$). The results from the killing assays are pooled from two ($n = 6$ for NK92, NK92–DNAM-1, NK92–DNAM-1^{R96A}, NK92–DNAM-1^{Y113A}, NK92–DNAM-1^{N186A}) or four (NK92–DNAM-1^{T188A}) independent experiments performed in triplicate.

Similar to the observations with DNAM-1 tetramer staining of K562 cells, (Fig. 4*C*), nectin-2 tetramers bound to each DNAM-expressing cell line with the exception of NK92$^{DNAM\text{-}1\ Y113A}$ cells (Fig. 5*A*). Given that NK92 cells preferentially kill via NKG2D, we performed the killing assays in the presence of the NKG2D-blocking antibody 1D11. Here, expression of WT DNAM-1 markedly improved NK cell cytotoxicity compared with the parental line, indicating that within this experimental system, killing was DNAM-1–dependent (Fig. 5*B*). Although the functional capacity of NK92 cells transduced with the control R96A DNAM-1 mutant was identical to that of WT DNAM-1, introduction of the Y113A mutation significantly reduced killing across all NK/target cell ratios, highlighting the importance of the conserved aromatic key residue (Fig. 5*B*). In contrast, mutations within DNAM-1 D2 (N186A and T188A) had no effect on NK cell killing at any effector/target cell ratio (Fig. 5*B*). Thus, in this NK cell assay, interactions derived from Asn-186 or its associated *N*-glycan chain did not influence DNAM-1–mediated cytotoxicity of nectin-2/Necl-5–expressing target cells.

Discussion

The nectin receptors are emerging as a critical regulatory checkpoint governing immune effector function. For example, overexpression of nectin-2 and Necl-5 on tumors has been reported to dampen T and NK cell responses via TIGIT and CD96 (16–19), whereas recognition of these same ligands by DNAM-1 promotes tumor immunosurveillance and clearance (15, 37–41). Moreover, DNAM-1 has been associated with a number of adverse autoimmune pathologies (42–44) and directly drives the allo-immune response in graft *versus* host disease (45). Thus, understanding the factors governing recognition within this paired receptor family has the potential to

Figure 4. Binding studies of DNAM-1 mutants. *A,* sensorgrams (*left*) and the corresponding equilibrium binding curves (*right*) showing the binding of nectin-2 and necl-5 to immobilized DNAM-1 and mutants thereof, as indicated. Sensorgrams and equilibrium binding curves show one representative of three (for WT DNAM-1 produced in HEK-293S and HEK-293T) or two (for all others) independent experiments, each performed in duplicate. Equilibrium dissociation constants (K_D) ± S.E. were calculated from the independent experiments. The amount of DNAM-1 coupled to the chip and the predicted maximal response (R_{max}) are indicated for each representative experiment shown. *ND* indicates not determined. *B–D,* binding of DNAM-1 mutant tetramers to K562 cells. *B,* K562 cells were stained with nectin-2– and necl-5–specific antibodies as indicated. *Histograms* of nectin-2 and necl-5 binding are representative of three independent experiments. For each panel, the *filled black histogram* is the isotype control, and the *filled gray histogram* is the specific antibody. The histograms are overlaid and are modal between samples. *C,* binding of WT and mutant DNAM tetramers to K562 cells. *Histograms* are representative of four independent experiments. The histograms have been offset and are modal. *D,* analysis of the median fluorescent intensity of the four independent tetramer staining experiments. **** indicates $p < 0.0001$ as determined using analysis of variance with Tukey's post hoc test.

inform future strategies for therapeutic intervention in a range of human diseases.

Within paired receptor families whose members compete with each other for ligand binding, the affinity of each receptor toward any given ligand constitutes a key factor governing the overall outcome of effector/target cell engagement. Here, inhibitory receptors are generally considered to bind to ligands with higher affinity than their activating counterparts, as evidenced within the KIRs (46) and the CTLA-4/CD28 (47) receptor systems. This bias favoring inhibition is likely important for the maintenance of immune tolerance toward healthy tissues under steady-state conditions. However, our binding data indicate that DNAM-1 binds to its ligands with an affinity in the same range as that of TIGIT and CD96 (2–10 μM) (29, 30). Thus, the nectin receptor axis likely represents a highly-sensitive system where relatively minor alterations in receptor/ligand expression levels could markedly impact immune cell activation.

The last few years have seen considerable progress in our understanding of the molecular basis underpinning nectin receptor recognition, in part due to the determination of multiple receptor–ligand complexes, including TIGIT/Necl-5 (31), TIGIT/nectin-2 (29), and CD96-D1/Necl-5 (30). Altogether, these studies have highlighted the important role that the D1 domain of each receptor, and in particular the lock and key motifs, plays in ligand binding. However, whereas TIGIT is composed of only a single Ig domain, DNAM-1 and CD96 possess two and three Ig domains, respectively, raising questions as to the evolutionary driving force behind this increased complexity, particularly because the isolated CD96 D1 domain is sufficient for ligand binding (30).

Here, we extend these findings by reporting the structure of the entire ectodomain of human DNAM-1 bound to Necl-5. DNAM-1 adopted an unusual stacked configuration of its two Ig domains that differed markedly from the linear arrangement observed within the nectin adhesion molecules. This collapsed architecture placed the D2 domain of DNAM-1 adjacent to Necl-5, such that Asn-186 and its associated *N*-glycan made direct interactions with the C–C′ loop of the ligand. Although we were only able to visualize a single GlcNAc moiety at the interface due to our inability to obtain crystals of natively glycosylated DNAM-1, MS-based glycopeptide and glycan analyses established that Asn-186 of recombinant DNAM-1 was extensively decorated with a heterogeneous mixture of large, complex *N*-glycans. Although our SPR and tetramer staining experiments demonstrated robust binding of fully glycosylated DNAM-1 to both nectin-2 and Necl-5, precisely how extended glycan chains attached to Asn-186 are accommodated at the relatively tight juncture between DNAM-1 D1, D2, and necl-5 D1 is at this stage unclear. Indeed, mutation of Asn-186 or removal of its associated *N*-glycan had no impact on DNAM-1 ligand–binding affinity or DNAM-1–mediated NK cell cytotoxicity. In this regard, it is important to note that Arg-185 of DNAM-1 D2 also makes interactions with Gly-70 of Necl-5. However, because these contacts were restricted to the main-chain atoms of the receptor and ligand, we were unable to test their functional importance using mutagenesis. Thus, although at this stage we have no evidence that DNAM-1 D2 contributes to ligand recognition, we cannot exclude this possibility entirely.

Our data raise new questions regarding the function of the D2 domain within the nectin receptor family. Because TIGIT comprises just a single extracellular Ig domain, it seems unlikely that the D2 domain is required as a structural scaffold to place the D1 domain in the appropriate position/orientation for ligand binding. Whether the D2 domain can impact recognition of other, as of yet unidentified, nectin receptor ligands or ancillary molecules that are directly associated with DNAM-1, such as leukocyte function-associated antigen-1 (LFA-1), will be an interesting avenue for future investigation. Moreover, it will also be insightful to identify whether the CD96 D2 domain adopts a configuration similar to that observed in DNAM-1, particularly because human CD96 exists as two isoforms that differ by a 16-residue insertion within the D2 domain, and this alteration has been reported to modulate Necl-5 binding (48).

Overall, the structure described herein is similar to that of mouse DNAM-1 bound to human Necl-5 recently reported by Wang *et al.* (32). The close overall architecture and binding affinity of human and mouse DNAM-1 indicate the evolutionarily conserved nature of this receptor system. However, mouse and human DNAM-1 have diverged somewhat in regard to primary amino acid sequence (53% identity within the ectodomain) and indeed the nature of many of the interactions were distinct. Although the D2 domain of both human and mouse DNAM-1 made interactions with Necl-5, mouse DNAM-1 did so via a solitary interaction derived from Glu-185 (equivalent to Gly-184 in human DNAM-1), whereas human DNAM-1 formed a more extensive interface that included Arg-185, Asn-186, and its associated *N*-glycan. Although the importance of Glu-185 in mouse DNAM-1/Necl-5 recognition was not formally tested, a truncated DNAM-1 construct comprising only the D1 domain exhibited reduced binding to Necl-5–expressing cells, leading the authors to conclude that the D2 domain modulated the interaction with Necl-5. This was in direct contrast to our binding and functional assays that indicated that mutation of contact residues within DNAM-1 D2 did not impact Necl-5 binding or DNAM-1 function. These results can be reconciled by our observation that we were unable to express properly folded DNAM-1 D1 in mammalian cells, indicating that the D2 domain might be important for stability of the receptor. Nevertheless, knowledge of these differences between human and mouse DNAM-1 will be important when interpreting data from mouse studies.

Experimental procedures

Cell culture

HEK-293T and HEK-293S cells were maintained at 37 °C and 5% CO_2 in Dulbecco's modified Eagle's medium (DMEM) supplemented with 4.5 g/liter L-glucose, 0.5 mg/ml penicillin/streptomycin/L-glutamine (Gibco), and 10% (v/v) heat-inactivated fetal calf serum (FCS) (Sigma). For protein expression, DMEM was supplemented with 2 mM L-alanyl-L-glutamine dipeptide (GlutaMAX, Gibco) and nonessential amino acids (Gibco), and the concentration of FCS was reduced to 2%. K562 cells were cultured in RPMI 1640 medium supplemented with

10% FCS, penicillin, and streptomycin. NK92 and NK92 transfectants were cultured in α-minimum essential media supplemented with 20% FCS, 12.5% horse serum, 0.2 mM inositol, 0.02 mM folic acid, 5 mM glutamate, 7.5% sodium bicarbonate, 1 M HEPES (pH 7.0), 1.43 mM β-mercaptoethanol, and 600 units/ml IL-2. K562 cells were seeded at 1×10^5 cells/ml and allowed to divide until cell density reached $\sim 1 \times 10^6$ cells/ml. NK92 cells were seeded at 5×10^5 cells/ml and allowed to divide until cell density reached 2×10^6 cells/ml.

Protein expression and purification

The construct encoding human DNAM-1 (amino acids 19–250) was codon-optimized for human expression (Integrated DNA Technologies) and cloned between AgeI and KpnI restriction sites into the pHLSec vector to include either a C-terminal hexa-histidine tag (for structural studies) or a consensus site for the biotin protein ligase enzyme (BirA) followed by a hexa-histidine tag (for SPR and tetramerization). The human nectin-2 ectodomain (residues 32–350) was cloned in the same manner. DNAM-1 (and mutants thereof) and nectin-2 were expressed via transient transfection in HEK-293S cells. For some SPR, tetramer staining, and MS experiments, WT DNAM-1 was also expressed in HEK-293T cells, where indicated. The human Necl-5 ectodomain (residues 32–350 and 28–334) was codon-optimized for expression in *Trichoplusia ni* (Integrated DNA Technologies) and cloned into the pFASTBac vector (Invitrogen) between XhoI and SpeI restriction sites to include a C-terminal hexa-histidine tag. The plasmid was incorporated into a recombinant baculovirus, and the viral titer was expanded in SF9 cells as described in the Bac-to-Bac manual (Invitrogen). Soluble Necl-5 was obtain by infecting Hi5 cells with 2% P3 virus. Secreted protein from mammalian and baculoviral systems was buffer-exchanged into 10 mM Tris-HCl (pH 8.0), 500 mM NaCl and purified via nickel-affinity and size-exclusion chromatography using a Superdex S200 16/600 column (GE Healthcare) in a buffer comprising 10 mM Tris-HCl (pH 8.0), 150 mM NaCl. For biotinylation, purified BirA-tagged DNAM-1 was buffer-exchanged into 10 mM Tris-HCl (pH 8.0) and biotinylated overnight at 4 °C.

Crystallization and data collection

For crystallization, purified DNAM-1 was enzymatically digested with endo H in the presence of 10 mM sodium citrate (pH 5.0) at 4 °C overnight, prior to being mixed with Necl-5 in a 1:1 molar ratio at a total concentration of 10 mg/ml. Crystals were obtained using the hanging-drop vapor diffusion method using a reservoir solution comprising 20% (v/v) PEG3350, 0.18 mM K_2SO_4, 10 mM EDTA and were cryo-protected in in the presence of 10% (v/v) glycerol. X-ray diffraction data were recorded on a Quantum-315 CCD detector at the MX2 beamline of the Australian Synchrotron. Data were integrated by MOSFLM and scaled using SCALA within the CCP4 suite of programs. Details of the data-processing statistics are given in Table S1.

Structure determination and refinement

The structure was determined by molecular replacement using Phaser. Isolated models for each of the Necl-5 D1, D2, and D3 domains were generated from the unliganded structure (PDB code 4FQP) (28) using PyMOL (Schrödinger, Inc.) and used as search models for the D1, D2, and D3 domains of Necl-5, respectively. Molecular replacement solutions for the DNAM-1 D1 and D2 domains were obtained using a model consisting of the isolated nectin-2 D1 (PDB code 5V52) as a search model. The structure was refined via iterative cycles of model building in Coot and refinement using Buster (http://globalphasing.com/buster/).[4] *N*-Linked glycans were manually incorporated into regions of positive density that correlated to the requisite sequence motif, N*X*(S/T), where *X* is any amino acid except proline. The final structure comprised two molecules of DNAM-1 and two molecules of Necl-5 within the asymmetric unit that were arranged into two heterodimers (heterodimer 1, chains A and C; heterodimer 2, chains B and D). Structural analysis was restricted to heterodimer 1 as the electron density surrounding chains A and C was better defined than that of chains B and D. The final structure refined to final R_{factor}/R_{free} values of 20.8 and 23.0. Details of the refinement statistics are given in Table S1. The structure factor file and associated atomic coordinates for the DNAM-1/Necl-5 structure have been deposited within the Protein Data Bank with the accession code 6O3O.

SPR

SPR experiments were performed using a BIAcore 3000 system (GE Healthcare) at 25 °C with a buffer comprising 10 mM Tris-HCl (pH 8.0), 150 mM NaCl, and 0.005% (v/v) surfactant P20. Varying response units of WT biotinylated DNAM-1 or mutants thereof (see Fig. 4 for details) were immobilized onto streptavidin-coated sensor chips (GE Healthcare), and flow cells were quenched with 10 μl of free D-biotin (1 mg/ml) at a flow rate of 5 μl/min prior to injection of analyte. Varying concentrations of soluble nectin-2 and Necl-5 were passed over the flow cells for 30–60 s, in duplicate, at a flow rate of 10 μl/min. The final responses were double-referenced by subtracting responses from an "empty" flow cell containing biotin-blocked streptavidin as well as from buffer-only injections. The responses at equilibrium were used to construct equilibrium binding curves that fit by a single-site binding model. The calculated equilibrium dissociation constants represent the mean $\pm$ S.E. of the mean from $n = 3$ (for WT DNAM-1 produced in HEK-293S and HEK-293T) or $n = 2$ (for all others) independent experiments. Data were analyzed with Scrubber2.0 (BioLogic Software, Campbell, ACT, Australia) and Prism 7.0 (GraphPad Software).

FACS analysis

K562 and NK92 cells were harvested and washed in PBS/FCS (1%), and Fc receptors were blocked using 10% normal goat serum. K562 cells were then washed and stained with DNAM-1 tetramers, anti-CD155 (TX24; Biolegend, San Diego), or anti-CD112 (TX31; Biolegend) for 30 min at 4 °C. After staining with DNAM-1 tetramers, cells were directly fixed by the addition of paraformaldehyde (10% in PBS) for 20 min at 4 °C. K562 cells

[4] Please note that the JBC is not responsible for the long-term archiving and maintenance of this site or any other third party hosted site.

stained with antibodies were not fixed. NK92 cells were stained with anti-DNAM antibody (11A8; Biolegend) or nectin-2 tetramers for 30 min at 4 °C. After staining with nectin-2 tetramers, cells were directly fixed by the addition of paraformaldehyde (10% in PBS) for 20 min at 4 °C. After staining/fixation, K562 and NK92 cells were washed twice in PBS/FCS and prepared for FACS. For acquisition, events were electronically gated on FSC-A *versus* FSC-H (singlets), followed by FSC-A and SSC-A (to exclude doublets and debris). Among the remaining populations, at least 5000 electronic events of interest were collected using an LSR-II or X-20 Fortessa (BD Biosciences).

Protein denaturation

The cysteine residues of recombinant human DNAM-1 expressed in HEK293T or HEK-293S cells were reduced using 10 mM aqueous DTT, 45 min at 56 °C, and then carbamidomethylated using 25 mM aqueous iodoacetamide, 30 min in the dark at 20 °C. The alkylation reaction was quenched using 30 mM aqueous DTT (final concentrations stated).

N-Glycan preparation

All reagents were obtained from Sigma unless otherwise stated. The water used for all experimental procedures was of ultra-high purity (MilliQ filtration system, Millipore). The DNAM-1 *N*-glycans were released and prepared for glycomics as described previously (49). In brief, DNAM-1 (20 μg) was immobilized in triplicate spots on a primed 0.45 μm polyvinylidene fluoride (PVDF) membrane (Merck-Millipore). The dried PVDF spots were stained with Direct Blue, excised, transferred to separate wells in a flat bottom polypropylene 96-well plate (Corning Life Sciences), blocked with 1% (w/v) polyvinylpyrrolidone in 50% (v/v) aqueous methanol, and washed with water. De-*N*-glycosylation was performed using 2 units of *Elizabethkingia miricola N*-glycosidase F (Promega) per 20 μg of DNAM-1 in 10 μl of water/well, 16 h at 37 °C. The released *N*-glycans were transferred into fresh tubes and hydroxylated by the addition of 100 mM aqueous ammonium acetate (pH 5), 1 h at 20 °C. The glycans were reduced using 1 M sodium borohydride in 50 mM aqueous potassium hydroxide, 3 h at 50 °C. The reaction was quenched using glacial acetic acid. Dual desalting of the reduced *N*-glycans was performed using first strong cation-exchange resin (where the *N*-glycans are not retained) and then porous graphitized carbon (PGC) (where *N*-glycans are retained) packed as micro-columns on top of C_{18} discs in P10 solid-phase extraction (SPE) formats. The *N*-glycans were eluted from the PGC micro-columns using 0.05% trifluoroacetic acid (TFA): 40% acetonitrile (ACN): 59.95% water (v/v/v), dried, and redissolved in 10 μl of water for LC-MS/MS analysis. Bovine fetuin was included as a sample handling and LC-MS/MS control.

N-Glycan analysis

The *N*-glycans were separated on a Hypercarb PGC column (particle size 3 μm, column length 100 mm, inner diameter 0.18 mm, Thermo Fisher Scientific) heated to 27 °C over an 83-min gradient of 0–45% (v/v) ACN (solvent B) in 10 mM aqueous NH_4HCO_3 (solvent A) at a flow of 2 μl/min delivered by a Dionex Ultimate-3000 HPLC (Dionex, CA). The glycans were detected using an LTQ Velos Pro ion trap mass spectrometer (Thermo Fisher Scientific) in negative ion polarity mode with a source voltage of 3.2 kV. The MS1 scan range was *m/z* 550–2000 with a zoom scan resolution of *m/z* 0.25 (FWHM). The automatic gain control (AGC) for the MS1 scan was 5×10^4 with a maximum accumulation time of 50 ms. Data-dependent tandem mass spectrometry (MS/MS) was performed using collision-induced dissociation at a normalized collision energy (NCE) of 33% of the 10 most abundant precursors in each MS1 scan. For the MS2 events, the resolution was set to *m/z* 0.35 (FWHM); the AGC was 2×10^4, and the maximum accumulation time was 300 ms. Dynamic exclusion was disabled. All MS and MS/MS spectra were acquired in profile mode. The LC-MS/MS instrument was tuned and calibrated, and its performance was bench-marked using bovine fetuin *N*-glycans prior to use. The raw LC-MS/MS data were browsed and annotated using Xcalibur version 2.2 (Thermo Fisher Scientific) using assisting software, *i.e.* GlycoMod and GlycoWorkBench, and manual *de novo* glycan sequencing as published previously (50). The relative abundances of the individual *N*-glycans were determined from relative area-under-the-curve (AUC) measurements based on extracted ion chromatograms (EICs) performed for the monoisotopic *m/z* values using Skyline (51).

N-Glycopeptide preparation

DNAM-1 was digested in solution using 1:30 (w/w, enzyme/substrate) sequencing-grade porcine trypsin (Promega) in 50 mM aqueous NH_4HCO_3 (pH 8.4), 16 h at 37 °C. The peptide mixture was dried and redissolved in 80% ACN, 1% TFA, 19% water(v/v/v). The tryptic glycopeptides and other hydrophilic DNAM-1 peptides were enriched using hydrophilic interaction LC–solid-phase extraction (HILIC-SPE) as described previously (52). In brief, HILIC-SPE micro-columns (10-mm column height) were prepared using zwitterionic HILIC (ZIC-HILIC) silica resin (10-μm particle size, 200 Å pore size, kindly provided by Merck-Millipore) packed into GELoader tips (Eppendorf) on top of C8 Empore SPE discs. The HILIC-SPE micro-columns were equilibrated using loading solvent consisting of 80% ACN, 1% TFA, 19% water (v/v/v). The peptide mixtures were loaded (and reloaded once) on the columns using an ordinary bench top microcentrifuge operated at low speed. The retained DNAM-1 peptides were eluted by applying 2× 50 μl of 1% (v/v) aqueous TFA, dried, and redissolved in 10 μl of water for LC-MS/MS analysis.

N-Glycopeptide analysis

The enriched *N*-glycopeptides were separated on a nano-flow reversed-phase Helo C18 column (particle size 2.7 μm, column length 100 mm, inner diameter 75 μm, Thermo Fisher Scientific) heated to 50 °C. A gradient over 70 min of 0–60% (v/v) solvent B (0.1% (v/v) formic acid (FA) in ACN) was applied (solvent A was 0.1% (v/v) aqueous FA). A constant flow rate of 450 nl/min was delivered by an Eksigent nano-400 LC system (SCIEX). The glycopeptides were detected using an Orbitrap Elite mass spectrometer (Thermo Fisher Scientific) in positive polarity mode with a source voltage of 3 kV. The MS1 scan range was *m/z* 500–200; AGC was 1×10^6, and the maximum

accumulation time was 50 ms. The 10 most abundant precursors in each MS1 scan were selected for data-dependent MS/MS acquisition (*m/z* 110–2000) using higher-energy C-trap dissociation (HCD) at an NCE of 35%. The AGC was 5×10^4, and the maximum accumulation time was 200 ms for the HCD-MS/MS events. Dynamic exclusion was enabled with a maximum repeat count of three for every 30 s. All MS and MS/MS spectra were acquired in profile mode. The LC-MS/MS instrument was tuned and calibrated, and its performance bench-marked using BSA peptides prior to use. The raw LC-MS/MS data were browsed and annotated using Xcalibur version 2.2 (Thermo Fisher Scientific) using assisting software, *i.e.* GPMAW version 10 (Lighthouse Data, Denmark) and Byonic version 2.3 (Protein Metrics) and manual *de novo* glycopeptide sequencing (53). The relative abundances of the individual *N*-glycopeptides were determined from relative AUC measurements based on monoisotopic *m/z* EICs performed manually using Xcalibur version 2.2 (Thermo Fisher Scientific).

Generation NK92–DNAM-1 cell lines

The full-length sequences of WT and mutated DNAM-1 were cloned into the MSCV plasmid and retroviral supernatants generated using HEK-293T cells. For NK92 transduction, 50 μg/ml retronectin was coated onto a nontreated plate for 2 h at room temperature prior to washing (2 times) and blocking with 2% BSA in PBS for 30 min. Plates were then washed with PBS (2 times), and viral supernatant was added to the wells after filtration through 0.45-μm filters. Virus was adhered to the plates by centrifugation at 1500 $\times$ *g* (2 h at room temperature). Supernatant was then removed, and the wells were washed with PBS, 0.1% BSA prior to addition of NK92 cells at 1×10^6 cells/ml. Cells and virus were integrated by centrifugation at 200 $\times$ *g* for 5 min at room temperature. NK92 cells infected with retrovirus were sorted on the basis of GFP expression. Populations were sorted until stable with insertion of DNAM-1 determined by FACS.

NK cell-killing assays

K562 cells were labeled with Cell Trace Violet according to the manufacturer's instructions (Thermo Fisher Scientific). NK92 cells were co-cultured with K562 cells in the presence of a saturating amount (10 μg/ml) of anti-NKG2D antibody (1D11; Biolegend). Different ratios of cells were added to U-bottom plates and centrifuged at 1400 rpm for 1 min. The co-cultures were then incubated for 4 h at 37 °C at which time they were washed and labeled with Zombie NR. For acquisition, events were electronically gated on FSC-A and SSC-A to detect live and dead cells. Effectors were excluded in the GFP channel, and targets were identified on the V450/50 channel. Among the remaining population in this channel, at least 200 viable electronic events of interest (CTV^+/Zombie NR^-) were collected using an LSR-II or X-20 Fortessa (BD Biosciences).

Author contributions—F. A. D. and G. M. W. formal analysis; F. A. D. validation; F. A. D., G. M. W., K. J. G., I. L., S. C., and Z. F. investigation; F. A. D. visualization; F. A. D. methodology; F. A. D. and R. B. writing-original draft; F. A. D., G. M. W., M. T.-A., D. M. A., J. R., and R. B. writing-review and editing; M. T.-A., D. M. A., J. R., and R. B. supervision; J. R. and R. B. conceptualization.

Acknowledgments—We thank the staff at the Monash Macromolecular Crystallization Facility and the Australian Synchrotron for their expert assistance. We also acknowledge staff from the A+ Flow Cytometry Core Facility for their expert assistance with cell sorting and acquisition.

References

1. Berry, R., Rossjohn, J., and Brooks, A. G. (2014) The Ly49 natural killer cell receptors: a versatile tool for viral self-discrimination. *Immunol. Cell Biol.* **92,** 214–220 CrossRef Medline
2. Burshtyn, D. N., and Morcos, C. (2016) The expanding spectrum of ligands for leukocyte Ig-like receptors. *J. Immunol.* **196,** 947–955 CrossRef Medline
3. Campbell, K. S., and Purdy, A. K. (2011) Structure/function of human killer cell immunoglobulin-like receptors: lessons from polymorphisms, evolution, crystal structures and mutations. *Immunology* **132,** 315–325 CrossRef Medline
4. Borrego, F., Masilamani, M., Marusina, A. I., Tang, X., and Coligan, J. E. (2006) The CD94/NKG2 family of receptors: from molecules and cells to clinical relevance. *Immunol. Res.* **35,** 263–278 CrossRef Medline
5. Kirkham, C. L., and Carlyle, J. R. (2014) Complexity and diversity of the NKR-P1:Clr (Klrb1:Clec2) recognition systems. *Front. Immunol.* **5,** 214 CrossRef Medline
6. Petrie, E. J., Clements, C. S., Lin, J., Sullivan, L. C., Johnson, D., Huyton, T., Heroux, A., Hoare, H. L., Beddoe, T., Reid, H. H., Wilce, M. C., Brooks, A. G., and Rossjohn, J. (2008) CD94–NKG2A recognition of human leukocyte antigen (HLA)-E bound to an HLA class I leader sequence. *J. Exp. Med.* **205,** 725–735 CrossRef Medline
7. Snyder, G. A., Brooks, A. G., and Sun, P. D. (1999) Crystal structure of the HLA–Cw3 allotype-specific killer cell inhibitory receptor KIR2DL2. *Proc. Natl. Acad. Sci. U.S.A.* **96,** 3864–3869 CrossRef Medline
8. Tormo, J., Natarajan, K., Margulies, D. H., and Mariuzza, R. A. (1999) Crystal structure of a lectin-like natural killer cell receptor bound to its MHC class I ligand. *Nature* **402,** 623–631 CrossRef Medline
9. Vivian, J. P., Duncan, R. C., Berry, R., O'Connor, G. M., Reid, H. H., Beddoe, T., Gras, S., Saunders, P. M., Olshina, M. A., Widjaja, J. M., Harpur, C. M., Lin, J., Maloveste, S. M., Price, D. A., Lafont, B. A., *et al.* (2011) Killer cell immunoglobulin-like receptor 3DL1-mediated recognition of human leukocyte antigen B. *Nature* **479,** 401–405 CrossRef Medline
10. Balaji, G. R., Aguilar, O. A., Tanaka, M., Shingu-Vazquez, M. A., Fu, Z., Gully, B. S., Lanier, L. L., Carlyle, J. R., Rossjohn, J., and Berry, R. (2018) Recognition of host Clr-b by the inhibitory NKR-P1B receptor provides a basis for missing-self recognition. *Nat. Commun.* **9,** 4623 CrossRef Medline
11. Diefenbach, A., Jamieson, A. M., Liu, S. D., Shastri, N., and Raulet, D. H. (2000) Ligands for the murine NKG2D receptor: expression by tumor cells and activation of NK cells and macrophages. *Nat. Immunol.* **1,** 119–126 CrossRef Medline
12. Aguilar, O. A., Berry, R., Rahim, M. M. A., Reichel, J. J., Popović, B., Tanaka, M., Fu, Z., Balaji, G. R., Lau, T. N. H., Tu, M. M., Kirkham, C. L., Mahmoud, A. B., Mesci, A., Krmpotić, A., Allan, D. S. J., *et al.* (2017) A viral immunoevasin controls innate immunity by targeting the prototypical natural killer cell receptor family. *Cell* **169,** 58–71.e14 CrossRef Medline
13. Berry, R., Ng, N., Saunders, P. M., Vivian, J. P., Lin, J., Deuss, F. A., Corbett, A. J., Forbes, C. A., Widjaja, J. M., Sullivan, L. C., McAlister, A. D., Perugini, M. A., Call, M. J., Scalzo, A. A., Degli-Esposti, M. A., *et al.* (2013) Targeting of a natural killer cell receptor family by a viral immunoevasin. *Nat. Immunol.* **14,** 699–705 CrossRef Medline
14. Martinet, L., and Smyth, M. J. (2015) Balancing natural killer cell activation through paired receptors. *Nat. Rev. Immunol.* **15,** 243–254 CrossRef Medline
15. Shibuya, A., Campbell, D., Hannum, C., Yssel, H., Franz-Bacon, K., McClanahan, T., Kitamura, T., Nicholl, J., Sutherland, G. R., Lanier, L. L., and Phillips, J. H. (1996) DNAM-1, a novel adhesion molecule involved in the

cytolytic function of T lymphocytes. *Immunity* **4,** 573–581 CrossRef Medline

16. Chan, C. J., Martinet, L., Gilfillan, S., Souza-Fonseca-Guimaraes, F., Chow, M. T., Town, L., Ritchie, D. S., Colonna, M., Andrews, D. M., and Smyth, M. J. (2014) The receptors CD96 and CD226 oppose each other in the regulation of natural killer cell functions. *Nat. Immunol.* **15,** 431–438 CrossRef Medline
17. Iguchi-Manaka, A., Kai, H., Yamashita, Y., Shibata, K., Tahara-Hanaoka, S., Honda, S., Yasui, T., Kikutani, H., Shibuya, K., and Shibuya, A. (2008) Accelerated tumor growth in mice deficient in DNAM-1 receptor. *J. Exp. Med.* **205,** 2959–2964 CrossRef Medline
18. Johnston, R. J., Comps-Agrar, L., Hackney, J., Yu, X., Huseni, M., Yang, Y., Park, S., Javinal, V., Chiu, H., Irving, B., Eaton, D. L., and Grogan, J. L. (2014) The immunoreceptor TIGIT regulates antitumor and antiviral CD8(+) T cell effector function. *Cancer Cell* **26,** 923–937 CrossRef Medline
19. Kurtulus, S., Sakuishi, K., Ngiow, S. F., Joller, N., Tan, D. J., Teng, M. W., Smyth, M. J., Kuchroo, V. K., and Anderson, A. C. (2015) TIGIT predominantly regulates the immune response via regulatory T cells. *J. Clin. Invest.* **125,** 4053–4062 CrossRef Medline
20. Liu, S., Zhang, H., Li, M., Hu, D., Li, C., Ge, B., Jin, B., and Fan, Z. (2013) Recruitment of Grb2 and SHIP1 by the ITT-like motif of TIGIT suppresses granule polarization and cytotoxicity of NK cells. *Cell Death Differ.* **20,** 456–464 CrossRef Medline
21. Stanietsky, N., Rovis, T. L., Glasner, A., Seidel, E., Tsukerman, P., Yamin, R., Enk, J., Jonjic, S., and Mandelboim, O. (2013) Mouse TIGIT inhibits NK-cell cytotoxicity upon interaction with PVR. *Eur. J. Immunol.* **43,** 2138–2150 CrossRef Medline
22. Zhang, Q., Bi, J., Zheng, X., Chen, Y., Wang, H., Wu, W., Wang, Z., Wu, Q., Peng, H., Wei, H., Sun, R., and Tian, Z. (2018) Blockade of the checkpoint receptor TIGIT prevents NK cell exhaustion and elicits potent anti-tumor immunity. *Nat. Immunol.* **19,** 723–732 CrossRef Medline
23. Fuchs, A., Cella, M., Giurisato, E., Shaw, A. S., and Colonna, M. (2004) Cutting edge: CD96 (tactile) promotes NK cell-target cell adhesion by interacting with the poliovirus receptor (CD155). *J. Immunol.* **172,** 3994–3998 CrossRef Medline
24. Gromeier, M., Lachmann, S., Rosenfeld, M. R., Gutin, P. H., and Wimmer, E. (2000) Intergeneric poliovirus recombinants for the treatment of malignant glioma. *Proc. Natl. Acad. Sci. U.S.A.* **97,** 6803–6808 CrossRef Medline
25. Masson, D., Jarry, A., Baury, B., Blanchardie, P., Laboisse, C., Lustenberger, P., and Denis, M. G. (2001) Overexpression of the CD155 gene in human colorectal carcinoma. *Gut* **49,** 236–240 CrossRef Medline
26. Oshima, T., Sato, S., Kato, J., Ito, Y., Watanabe, T., Tsuji, I., Hori, A., Kurokawa, T., and Kokubo, T. (2013) Nectin-2 is a potential target for antibody therapy of breast and ovarian cancers. *Mol. Cancer* **12,** 60 CrossRef Medline
27. Sloan, K. E., Eustace, B. K., Stewart, J. K., Zehetmeier, C., Torella, C., Simeone, M., Roy, J. E., Unger, C., Louis, D. N., Ilag, L. L., and Jay, D. G. (2004) CD155/PVR plays a key role in cell motility during tumor cell invasion and migration. *BMC Cancer* **4,** 73 CrossRef Medline
28. Harrison, O. J., Vendome, J., Brasch, J., Jin, X., Hong, S., Katsamba, P. S., Ahlsen, G., Troyanovsky, R. B., Troyanovsky, S. M., Honig, B., and Shapiro, L. (2012) Nectin ectodomain structures reveal a canonical adhesive interface. *Nat. Struct. Mol. Biol.* **19,** 906–915 CrossRef Medline
29. Deuss, F. A., Gully, B. S., Rossjohn, J., and Berry, R. (2017) Recognition of nectin-2 by the natural killer cell receptor T cell immunoglobulin and ITIM domain (TIGIT). *J. Biol. Chem.* **292,** 11413–11422 CrossRef Medline
30. Deuss, F. A., Watson, G. M., Fu, Z., Rossjohn, J., and Berry, R. (2019) Structural basis for CD96 immune receptor recognition of Nectin-like protein-5, CD155. *Structure* **27,** 219–228.e3 CrossRef Medline
31. Stengel, K. F., Harden-Bowles, K., Yu, X., Rouge, L., Yin, J., Comps-Agrar, L., Wiesmann, C., Bazan, J. F., Eaton, D. L., and Grogan, J. L. (2012) Structure of TIGIT immunoreceptor bound to poliovirus receptor reveals a cell–cell adhesion and signaling mechanism that requires cis-trans receptor clustering. *Proc. Natl. Acad. Sci. U.S.A.* **109,** 5399–5404 CrossRef Medline
32. Wang, H., Qi, J., Zhang, S., Li, Y., Tan, S., and Gao, G. F. (2019) Binding mode of the side-by-side two-IgV molecule CD226/DNAM-1 to its ligand CD155/Necl-5. *Proc. Natl. Acad. Sci. U.S.A.* **116,** 988–996 CrossRef Medline
33. Lázár-Molnár, E., Yan, Q., Cao, E., Ramagopal, U., Nathenson, S. G., and Almo, S. C. (2008) Crystal structure of the complex between programmed death-1 (PD-1) and its ligand PD-L2. *Proc. Natl. Acad. Sci. U.S.A.* **105,** 10483–10488 CrossRef Medline
34. Mohammed, F., Stones, D. H., Zarling, A. L., Willcox, C. R., Shabanowitz, J., Cummings, K. L., Hunt, D. F., Cobbold, M., Engelhard, V. H., and Willcox, B. E. (2017) The antigenic identity of human class I MHC phosphopeptides is critically dependent upon phosphorylation status. *Oncotarget* **8,** 54160–54172 CrossRef Medline
35. Foster, C. E., Colonna, M., and Sun, P. D. (2003) Crystal structure of the human natural killer (NK) cell activating receptor NKp46 reveals structural relationship to other leukocyte receptor complex immunoreceptors. *J. Biol. Chem.* **278,** 46081–46086 CrossRef Medline
36. Maxwell, K. F., Powell, M. S., Hulett, M. D., Barton, P. A., McKenzie, I. F., Garrett, T. P., and Hogarth, P. M. (1999) Crystal structure of the human leukocyte Fc receptor, FcγRIIa. *Nat. Struct. Biol.* **6,** 437–442 CrossRef Medline
37. Cho, D., Shook, D. R., Shimasaki, N., Chang, Y. H., Fujisaki, H., and Campana, D. (2010) Cytotoxicity of activated natural killer cells against pediatric solid tumors. *Clin. Cancer Res.* **16,** 3901–3909 CrossRef Medline
38. Gilfillan, S., Chan, C. J., Cella, M., Haynes, N. M., Rapaport, A. S., Boles, K. S., Andrews, D. M., Smyth, M. J., and Colonna, M. (2008) DNAM-1 promotes activation of cytotoxic lymphocytes by nonprofessional antigen-presenting cells and tumors. *J. Exp. Med.* **205,** 2965–2973 CrossRef Medline
39. Lakshmikanth, T., Burke, S., Ali, T. H., Kimpfler, S., Ursini, F., Ruggeri, L., Capanni, M., Umansky, V., Paschen, A., Sucker, A., Pende, D., Groh, V., Biassoni, R., Höglund, P., Kato, M., *et al.* (2009) NCRs and DNAM-1 mediate NK cell recognition and lysis of human and mouse melanoma cell lines *in vitro* and *in vivo*. *J. Clin. Invest.* **119,** 1251–1263 CrossRef Medline
40. Ramsbottom, K. M., Hawkins, E. D., Shimoni, R., McGrath, M., Chan, C. J., Russell, S. M., Smyth, M. J., and Oliaro, J. (2014) Cutting edge: DNAX accessory molecule 1-deficient CD8+ T cells display immunological synapse defects that impair antitumor immunity. *J. Immunol.* **192,** 553–557 CrossRef Medline
41. Verhoeven, D. H., de Hooge, A. S., Mooiman, E. C., Santos, S. J., ten Dam, M. M., Gelderblom, H., Melief, C. J., Hogendoorn, P. C., Egeler, R. M., van Tol, M. J., Schilham, M. W., and Lankester, A. C. (2008) NK cells recognize and lyse Ewing sarcoma cells through NKG2D and DNAM-1 receptor dependent pathways. *Mol. Immunol.* **45,** 3917–3925 CrossRef Medline
42. Hafler, J. P., Maier, L. M., Cooper, J. D., Plagnol, V., Hinks, A., Simmonds, M. J., Stevens, H. E., Walker, N. M., Healy, B., Howson, J. M., Maisuria, M., Duley, S., Coleman, G., Gough, S. C., International Multiple Sclerosis Genetics Consortium (IMSGC), *et al.* (2009) CD226 Gly307Ser association with multiple autoimmune diseases. *Genes Immun.* **10,** 5–10 CrossRef Medline
43. Löfgren, S. E., Delgado-Vega, A. M., Gallant, C. J., Sánchez, E., Frostegård, J., Truedsson, L., de Ramón Garrido, E., Sabio, J. M., González-Escribano, M. F., Pons-Estel, B. A., D'Alfonso, S., Witte, T., Lauwerys, B. R., Endreffy, E., Kovács, L., *et al.* (2010) A 3′-untranslated region variant is associated with impaired expression of CD226 in T and natural killer T cells and is associated with susceptibility to systemic lupus erythematosus. *Arthritis Rheum.* **62,** 3404–3414 CrossRef Medline
44. Reinards, T. H., Albers, H. M., Brinkman, D. M., Kamphuis, S. S., van Rossum, M. A., Girschick, H. J., Wouters, C., Hoppenreijs, E. P., Saurenmann, R. K., Hinks, A., Ellis, J. A., Bakker, E., Verduijn, W., Slagboom, P., Huizinga, T. W., *et al.* (2015) CD226 (DNAM-1) is associated with susceptibility to juvenile idiopathic arthritis. *Ann. Rheum. Dis.* **74,** 2193–2198 CrossRef Medline
45. Nabekura, T., Shibuya, K., Takenaka, E., Kai, H., Shibata, K., Yamashita, Y., Harada, K., Tahara-Hanaoka, S., Honda, S., and Shibuya, A. (2010) Critical role of DNAX accessory molecule-1 (DNAM-1) in the development of acute graft-versus-host disease in mice. *Proc. Natl. Acad. Sci. U.S.A.* **107,** 18593–18598 CrossRef Medline

46. Saunders, P. M., Vivian, J. P., O'Connor, G. M., Sullivan, L. C., Pymm, P., Rossjohn, J., and Brooks, A. G. (2015) A bird's eye view of NK cell receptor interactions with their MHC class I ligands. *Immunol. Rev.* **267,** 148–166 CrossRef Medline
47. Sansom, D. M. (2000) CD28, CTLA-4 and their ligands: who does what and to whom? *Immunology* **101,** 169–177 CrossRef Medline
48. Meyer, D., Seth, S., Albrecht, J., Maier, M. K., du Pasquier, L., Ravens, I., Dreyer, L., Burger, R., Gramatzki, M., Schwinzer, R., Kremmer, E., Foerster, R., and Bernhardt, G. (2009) CD96 interaction with CD155 via its first Ig-like domain is modulated by alternative splicing or mutations in distal Ig-like domains. *J. Biol. Chem.* **284,** 2235–2244 CrossRef Medline
49. Jensen, P. H., Karlsson, N. G., Kolarich, D., and Packer, N. H. (2012) Structural analysis of *N*- and *O*-glycans released from glycoproteins. *Nat. Protoc.* **7,** 1299–1310 CrossRef Medline
50. Everest-Dass, A. V., Jin, D., Thaysen-Andersen, M., Nevalainen, H., Kolarich, D., and Packer, N. H. (2012) Comparative structural analysis of the glycosylation of salivary and buccal cell proteins: innate protection against infection by *Candida albicans*. *Glycobiology* **22,** 1465–1479 CrossRef Medline
51. Ashwood, C., Lin, C.-H., Thaysen-Andersen, M., and Packer, N. H. (2018) Discrimination of isomers of released *N*- and *O*-glycans using diagnostic product ions in negative ion PGC-LC-ESI-MS/MS. *J. Am. Soc. Mass Spectrom.* **29,** 1194–1209 CrossRef Medline
52. Mysling, S., Palmisano, G., Højrup, P., and Thaysen-Andersen, M. (2010) Utilizing ion-pairing hydrophilic interaction chromatography solid phase extraction for efficient glycopeptide enrichment in glycoproteomics. *Anal. Chem.* **82,** 5598–5609 CrossRef Medline
53. Sumer-Bayraktar, Z., Nguyen-Khuong, T., Jayo, R., Chen, D. D., Ali, S., Packer, N. H., and Thaysen-Andersen, M. (2012) Micro- and macroheterogeneity of *N*-glycosylation yields size and charge isoforms of human sex hormone binding globulin circulating in serum. *Proteomics* **12,** 3315–3327 CrossRef Medline